

## Flexible and Printed Electronics



### PAPER

# Aerosol jet printing of PEDOT:PSS for large area flexible electronics

RECEIVED  
23 September 2019

REVISED  
20 November 2019

ACCEPTED FOR PUBLICATION  
13 December 2019

PUBLISHED  
27 January 2020

Giuseppe Tarabella<sup>1,3</sup> , Davide Vurro<sup>2</sup>, Stefano Lai<sup>1</sup>, Pasquale D'Angelo<sup>2,3</sup>, Luca Ascari<sup>1</sup> and Salvatore Iannotta<sup>2</sup>

<sup>1</sup> Camlin Italy Srl, Via Budellungo 2, I-43124, Parma, Italy

<sup>2</sup> Inst. of Materials for Electronics and Magnetism (IMEM-CNR), Campus Area delle Scienze 37A, I-43127, Parma, Italy

<sup>3</sup> These authors equally contributed to this work.

E-mail: [l.ascari@camlintechnologies.com](mailto:l.ascari@camlintechnologies.com)

**Keywords:** aerosol jet printing, PEDOT:PSS, overspray, organic electrochemical transistor, organic bioelectronics

Supplementary material for this article is available [online](#)

### Abstract

We investigate and optimize the Aerosol Jet Printing of PEDOT:PSS by studying the role of parameters determining the final quality of the printed features. Printing thin films of organic materials requires a high control in the deposition process to control the morphology/structure of the films that determine the electrical and functional performance of organic devices. We studied aerosol jet printed lines of the PEDOT:PSS semiconductive polymer on flexible Kapton substrates. We choose the focus ratio, defined as the ratio between the sheath and carrier gas flow rates, as the main parameter that best characterizes the process and hence the characteristics of printed lines. A detailed analysis of the line width and thickness, as a function of the focus ratio and carrier gas flow for different nozzle sizes and sheath gas flow rates, is reported. The edge profile definition of printed PEDOT:PSS lines has been found to be affected by a combination of overspray, typical of aerosol deposition, and pinholes due to the Kapton/PEDOT:PSS interaction, while their core profile results to be almost defects free. An optimal printing window for different nozzle sizes has been determined in terms of a minimization of overspray/pinholes effects with respect to the whole line width. Finally, an array of whole-plastic, planar Organic Electrochemical Transistors, having both the channel and the gate electrode made of PEDOT:PSS, has been manufactured using the best combination of process parameters. Transistors have been characterized for different channel/gate area ratios and the transconductance analysed as a function of channel to gate area.

### 1. Introduction

In last decades relevant efforts have been devoted to design and implement new printing techniques fostering rapid prototyping of various geometries, overcoming limitations of traditional and cost-consuming photolithographic methods [1]. Direct-Write (DW) printing is an Additive Manufacturing (AM) technique suitable to deposit features onto different kinds of substrate materials, allowing CAD-based rapid prototyping of various geometries [2, 3]. Inkjet printing is the best known DW technique, already exploited to print flexible circuits, including transducers for biosensing and biopotential recording [4]. Aerosol Jet Printing (AJP) represents a promising extension of Inkjet, in terms of (i) larger set of printable materials (including also viscous insulators), (ii) easier prototyping of ink

formulation [3], (iii) printing on 3D surface [5, 6], (iv) improved resolution of printed features with size down to 8  $\mu\text{m}$  [7], (v) open to implementation towards 4D printing [8]. AJP offers several additional potential advantages compared to the Inkjet [9], particularly in the area of microelectronics and large area, flexible/wearable electronics [1, 10]. AJP has been successfully used for manufacturing antennae made of inorganic materials [6], to print parts of Organic Field Effect Transistors [11], passive components [3], and ZnO-based photodetectors [12]. Recently, AJP has also been used to print bio-materials [13], and for stretchable and flexible electronics [14]. Although AJP has already demonstrated advantages, including reproducibility and printing resolution, minimization and control of edge profile instabilities of the printed lines, generally referred as overspray (OS), continues to be a challenging

**Table 1.** Review from literature of process parameters used for printing PEDOT:PSS by AJP. All depositions were carried out using UA.

PEDOT: PSS ink	LW ( $\mu\text{m}$ )	Gas flows SG/ CG (sccm)	Nozzle ( $\mu\text{m}$ )	Plate Temp. ( $^{\circ}\text{C}$ )	Substrate	Application	References
Bytron P	26	—	—	60	Kapton	TFT	[24]
PEDOT:PSS	100	—	—	50	Kapton	TFT	[25]
PH500	50	—	—	60	PET	EGTs	[26]
PH500	100	40/20	150	60	Kapton	EGTs	[27]
PH500	83	40/20	150	60	SiO <sub>2</sub> /Si wafer	EGTs	[11]
PH1000	86	40/20	150	60	SiO <sub>2</sub> /Si wafer	EGTs	[28]
C-NANO-NV	70	40/40	150	40	Kapton	Four points	[7]
V2JET	—	60/30	250	60	PET	Resistors	[3]
PH1000	126	35/25	—	60	SiO <sub>2</sub> /Si wafer	EGTs	[29]

open issue. In AJP, as well as ink jet printing, the optimization of process parameters for every specific ink, is a challenging task because it depends on several parameters, mainly from the substrate/ink compatibility, as well as on the deposition system's parameters, other than on cleaning protocols or fine contaminations. A standardized procedure to optimize and control process parameters is missing, and each ink is printed with an optimization focused on specific applications. In this work, we provide a recipe for the aerosol printing of a specific couple substrate/ink, i.e. PEDOT:PSS/Kapton. A standardized approach has been proposed very recently, also exploiting machine learning analysis [15]. Hydrophilicity/hydrophobicity of the substrate, environmental and possible non-thermodynamic equilibrium conditions of the process upon deposition of organic thin films from liquid precursors [16, 17], are some of the factors that have to be taken into account to achieve a reproducible printing quality. However, despite being already identified as important factors of the production process, their investigation is far from being satisfactory and requires further thorough studies to achieve the needed level of confidence and performance. Even though OS issues have been identified on miniaturized applications where cross-talking effects arising between close and adjacent structures are critical [18], only a few studies have systematically analysed OS [10], and discussed its causes [19]. Among these, the work by *Chen et al* gives a comprehensive interpretation of OS based on the analysis of the influence of printing parameters on the deposition of an insulating material (Norland Electronic Adhesives, NEA, 121) [20].

In this framework, here, we contribute to the comprehension of the mechanisms and to the control of OS, investigating printing quality, thus extending the state of the art to organic aqueous inks printed on plastic, flexible substrates suitable for microelectronics printing [10]. We hence choose a substrate widely used in flexible electronics, a polyimide thin film (Kapton<sup>®</sup>), over which we print PEDOT:PSS inks, which is one of the best performing [21, 22], semiconducting polymers available for organic electronics.

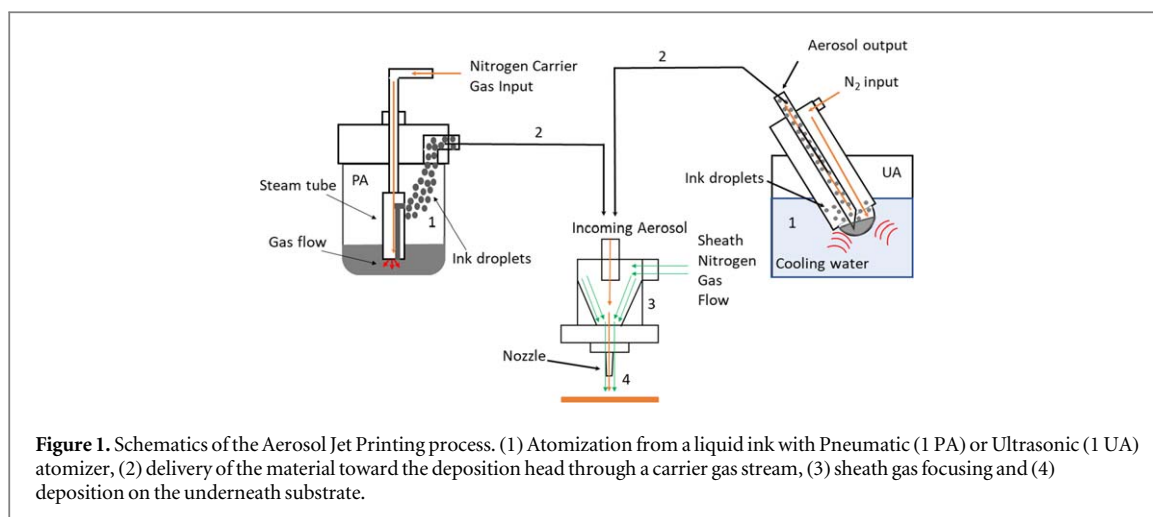
Table 1 summarizes synthetically the state of the art in literature on PEDOT:PSS printed by AJP on three different substrates (Kapton, PET and SiO<sub>2</sub>/Si).

Table 1 is aimed at giving an easy fast reference guide to the reader. The reported works only explore just one set of process parameters, as their major aim is the manufacturing of specific organic devices instead of a complete characterization of the PEDOT:PSS printing process. A complete characterization of the printing quality for the PEDOT:PSS/Kapton system is in fact still missing, so that AJP cannot be yet considered as a method fully exploitable for flexible and wearable electronics. Our work is aimed at assessing the PEDOT:PSS writing quality on Kapton, quantitatively evaluating instabilities of line features in terms of an ill-defined line profile that is mainly ascribed to both OS phenomena and emerging pinholes occurring in the proximity of the line edges. OS is determined by the formation of small ink droplets within the aerosol jet that, deviating from the centre of the gas flow, are being deposited on the substrate at a variable distance away from the core of the line, contributing to an uncontrolled width of the lines [20, 23]. Pinholes can be ascribed in our case to PEDOT:PSS/Kapton interaction. Our analysis of printed lines instabilities is accordingly referred to the combined effect of holes formations and overspray (*hOS*).

The paper gives first the experimental setup, materials and methods. Experimental results and the related discussion are presented in the second part. The final section shows a set of organic electrochemical transistors (OECTs) made of PEDOT:PSS, that are the first whole-organic aerosol jet printed OECT reported in literature. We showed a fabrication process consisting of three layers of deposition, for: (1) contacting circuitry (Silver ink), (2) organic active layers (PEDOT:PSS ink) and (3) protection/passivation layer (NEA 121 ink).

### 1.1. The AJP

For a detailed introduction to the operating principles of the AJP we refer the reader to the paper by *E. Secor* [23]. Here we give only an overall synthetic description that is needed to make the paper and the discussion easier to be understood. Figure 1 shows a schematic of the AJP that is based on four main steps of process: (1) atomization from a liquid ink in which a mist of the material, the aerosol, is generated through a



pneumatic or ultrasonic atomizer; (2) the atomized material is then delivered to the printing head through a carrier gas flow (nitrogen); (3) the aerosolized material seeded in the gas flow is surrounded by a sheath gas flow that confines and collimates the aerosol stream and (4) it is focused inside the nozzle for the deposition on the underneath substrate at a distance varying between 3 and 5 mm.

In more detail, the atomization step is required to produce the aerosol phase from the liquid ink, determining droplets with a diameter size in the range of 1–5  $\mu\text{m}$  [23]. We measured the deposit size from individual droplets by SEM, finding an average splat diameter of 1.5  $\mu\text{m}$  (figure SI 2D is available online at [stacks.iop.org/FPE/5/014005/mmedia](https://stacks.iop.org/FPE/5/014005/mmedia)). During the printing run, the substrate is kept at a constant temperature with a controlled-temperature plate. Depending on the ink/material properties, the temperature of the platen (moving stage) allows the solvent to evaporate quickly just after droplets impinging. As already mentioned, the mist is generated by an ultrasonic (UA) or a pneumatic atomizer (PA), capable of atomizing inks with viscosities from 1 to 10 cPs, and from 10 to 1000 cPs, respectively, a range much wider than in Inkjet printing [9]. In the UA, an ultrasonic wave generates droplets of ink through a surface acoustic wave. Heavier droplets recombine in the liquid phase, while lighter droplets get captured by the gas carrier flow and addressed toward the printing head, through a delivery tube (the mist tube). In the PA, a gas flow at high pressure (from hundreds of sccm up to 2000 sccm) is used to generate droplets. PA is equipped with a waste reservoir connected to a virtual impactor, where the smaller droplets are trapped by means of an Exhaust Gas Flow. Gas flow parameters settings i.e. flow rates of carrier gas (CGFR), exhaust (EGF) and sheath flow (SGFR), depend strongly on the ink viscosity. Once formed, the aerosol is carried toward the deposition head through the gas carrier flow, via the mist tube. Once inside the deposition head, the atomized material is surrounded by the sheath gas flow, whose function is to aerodynamically focus the material flow and,

hence, to control the spot size. The nozzle tip can be kept at a distance from the substrate of 3–5 mm. At the exit of the nozzle, the flow stream impinges on the underneath substrate depositing the material. AJP belongs to the family of Direct Writing Additive Manufacturing Technologies, and it is a CAD-driven technique, where the toolpath of patterns is designed by the AutoCAD software controlling the movement of the plate.

## 2. Materials and methods

All the experiments were carried out with a commercial Aerosol Jet Printer (AJP 200, Optomec Inc.) equipped both with an Ultrasonic (UA) and a Pneumatic Atomizer (PA). The Clevios P JET N V2, with a viscosity of 5cPs, is an inkjet formulation of PEDOT:PSS, suitable for ultrasonic aerosol printing and was purchased from Heraeus GmbH. The JET N V2 ink consists of a dispersion in PSS phase of PEDOT clusters with nominal average diameter <20 nm [30], that is doped with 8% w/v of Ethylene Glycol already optimized for inkjet printers. The Silver ink used was the Prelect<sup>®</sup> TPS 50G2 (from Clariant), consisting of silver particles of approximately 10–20 nm in diameter, dispersed in ethylene glycol. Silver Clariant ink has a viscosity of 12 cPs. The Ultrasonic Atomizer is suitable to print inks with a maximum viscosity of 10cPs; hence the Silver Clariant ink was diluted 1:1 v/v in DI Water to lower the final viscosity below 10 cPs. As passivation material, we used the Norland adhesive NEA 121, having a high viscosity of 300 cPs, that is printable by using the Pneumatic Atomizer. Both the silver-ink and PEDOT:PSS formulations were printed using the ultrasonic atomizer.

Using the UA, we loaded inside a glass vial 2 ml of the ink just before every printing run. The vial was immersed into a stabilizer water bath keeping the temperature of the ink at the constant value of 20 °C. Ultrasonic current was set to the constant value of 0.5 mA. We used commercially available Kapton foils,

purchased from RS Electronics, as substrates (75  $\mu\text{m}$  thickness). Substrates were cleaned with Acetone, IPA, DI-Water, followed by a plasma-oxygen treatment (2 min, 30 W) before each printing run, in order to enhance the hydrophilicity of the surface and allow the ink to spread and adhere easier over the surface. Untreated substrates show a relevant surface hydrophobicity that makes the ink adhesion onto the substrate quite poor and hence often producing discontinuous lines. During every printing session the speed of the stage ( $1 \text{ mm s}^{-1}$ ) and the distance between the tip of the nozzle and the substrate ( $d = 3 \text{ mm}$ ), are kept constant. Preliminary tests show that the chosen distance  $d$  was the optimal for a better film homogeneity. Four different nozzles with diameters  $D_n = 100, 150, 200$  and  $300 \mu\text{m}$  have been used for the deposition of the PEDOT:PSS lines. Drifting issues, consisting of a worsening in the quality of the printing features over the time, represent a critical drawback in AJP. To exclude drifting effects on the characterization of PEDOT:PSS printed lines, we used to perform a continuous printing for 5 min before the first printing run. We performed a preliminary checking by controlling how to optimize the deposition in terms of a negligible drift. SEM images of two lines printed at the beginning and after 15 min of continuous printing indicated that the drifting effects are minimal and quantitatively evaluated by a reduction of the line width that, for instance, is less than 2.8% in the case of a  $200 \mu\text{m}$  nozzle at  $\text{CGFR} = 26 \text{ sccm}$  and  $\text{FR} = 3$ . As the timescale of our experiments is of about 1 min, drifting effects are excluded.

Printed lines have been characterized by acquiring SEM microscopy (Auriga Compact), while line width (LW) and instabilities have been quantitatively evaluated through the open-source imaging software Gwyddion 2.53. The Gwyddion analysis (roughness tool) consists of evaluating and comparing the roughness and the shape of each line parallel to the horizontal axis of a SEM image,  $512 \times 512 \text{ px res}$ , which defines the profiles of both the cross-sectional shape of the printed line and the substrate around the same line that is not covered by PEDOT:PSS. Both roughness and shape of the substrate/line profiles can be simultaneously obtained. A statistical analysis has been carried out averaging individual profiles of 128 different horizontal lines composing the central region of the analysed SEM image (see figures 2(A) and (B)). Line thicknesses have been also measured by a profilometer (Tencor P10) to calibrate the profiles obtained by Gwyddion software. The extracted line parameters have been plotted as a function of the Focus Ratio (FR) that, as already mentioned, represents the main figure of merit for characterizing line quality features, and is defined as the ratio between ShGFR and CGFR [3, 18]. OS is another important factor affecting the printing quality. It can be quantitatively defined as:  $\text{OS} = \frac{\text{LW}_{\text{illdef}}}{\text{LW}}$ , where  $\text{LW}_{\text{illdef}}$  is the width of the ill-defined part of the

printed line and LW is its whole width. Fine control of OS is a critical step in the AJP process because it can cause unwanted overlapping of electrical paths, leading to short-circuit or to a not-well defined edge in device geometries, limiting the final resolution of the fabrication process.

We fabricated a series of OEECTs where all the features were realized by the AJ200 aerosol jet printer. We designed a planar architecture consisting of three layers respectively defining (1) the silver source and drain contacts (active device channel definition) and interconnects, (2) the transistor channel and the gate electrode made of PEDOT:PSS and (3) a protective/passivation layer made of the NEA 121 adhesive. The device geometry has been conceived for an electrical connection to the measurement station based on zero insertion force (ZIF) connectors.

The ratio between the gate and channel areas was varied from 2:1 to 5:1 [31], while the distance between the channel and gate was fixed at  $150 \mu\text{m}$  for all the printed devices. For each of the gate/channel area ratio, three OEECTs were printed. The aspect ratio of designed OEECT channel (width/length,  $W/L$ ) is 1 ( $W = 200 \mu\text{m}$ ;  $L = 200 \mu\text{m}$ ). Process parameters were chosen to obtain a  $200 \text{ nm}$  thick PEDOT:PSS layers. Electrical characterizations were performed using a National Instruments PXIe-8370 system equipped with a PXIe-4145 source measure unit (SMU), used to apply  $V_{\text{ds}}$  and  $V_{\text{gs}}$  at the OEECTs terminals (Source, Drain and Gate) and measure simultaneously the channel and gate currents,  $I_{\text{ds}}$  and  $I_{\text{gs}}$ , with a scan time of  $0.1 \text{ s}$ . The output curves ( $I_{\text{ds}}$  versus  $V_{\text{ds}}$ ) were measured by varying  $V_{\text{ds}}$  in the range from  $0$  to  $-0.6 \text{ V}$  in steps of  $0.05 \text{ V}$  for fixed  $V_{\text{gs}}$  (from  $0$  to  $0.8 \text{ V}$ , steps of  $0.1 \text{ V}$ ). The transfer curves ( $I_{\text{ds}}$  versus  $V_{\text{gs}}$ ) were acquired by biasing the source-drain terminals at  $V_{\text{ds}} = -0.1 \text{ V}$  and by varying the gate voltage  $V_{\text{gs}}$  from  $-0.2$  to  $0.8 \text{ V}$ , in steps of a  $0.05 \text{ V}$ , at a scan time rate of  $0.05 \text{ s}$ . All measurements were done in an aqueous solution of  $\text{NaCl } 150 \text{ mM}$ , used as the gate electrolyte and confined by a printed artificial ring-shaped well made of NEA121, surrounding the channel and gate electrodes. Before each measurement, the PEDOT:PSS channel was hydrated in DI-water to allow the full water swelling to optimize the porosity and the formation of water channels inside the PEDOT:PSS microstructure [32]. This procedure confers the needed reproducibility during all the measurement sessions [33]. Three repeated transfer curves were measured for each of the fabricated devices. Transconductance  $g_m$ , which is a figure of merit measuring the OEECT amplification, was calculated by plotting the derivative of the transfer curve ( $g_m = dI_{\text{ds}}/dV_{\text{gs}}$ ). The transit time of holes ( $\tau_e$ ) in the PEDOT:PSS channel was estimated by recording the variation of  $I_{\text{ds}}(t)$  (at  $V_{\text{ds}} = -0.1 \text{ V}$ ) upon application of four constant gate currents, ( $I_{\text{gs}} = 100 \text{ nA}, 500 \text{ nA}, 1 \mu\text{A}$  and  $5 \mu\text{A}$ ), as [34, 35]:

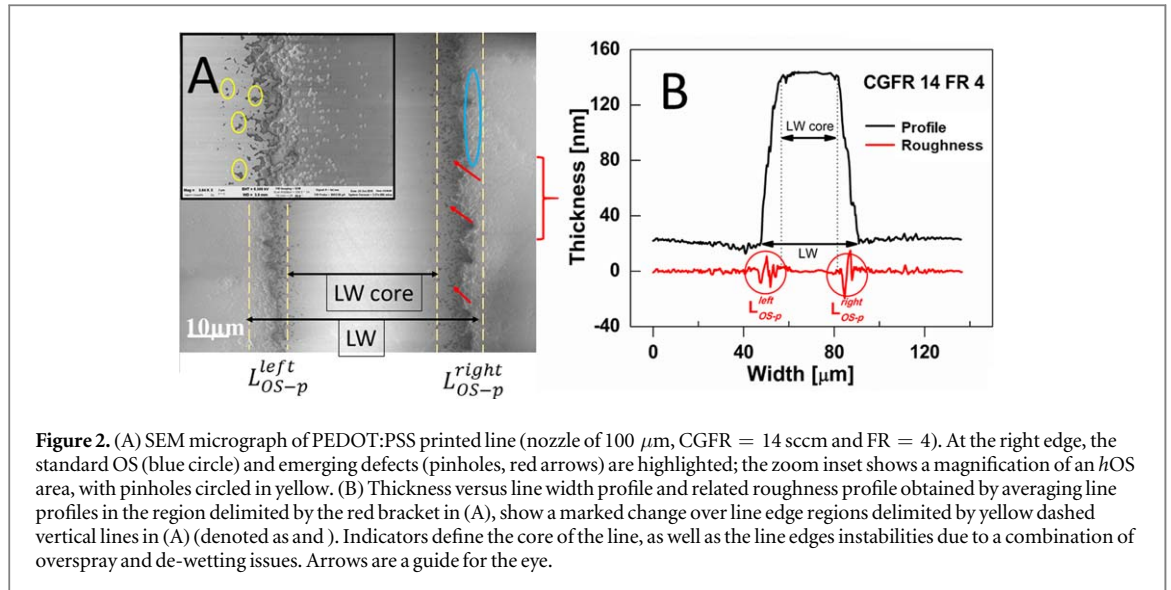


**Figure 2.** (A) SEM micrograph of PEDOT:PSS printed line (nozzle of 100  $\mu\text{m}$ , CGFR = 14 sccm and FR = 4). At the right edge, the standard OS (blue circle) and emerging defects (pinholes, red arrows) are highlighted; the zoom inset shows a magnification of an hOS area, with pinholes circled in yellow. (B) Thickness versus line width profile and related roughness profile obtained by averaging line profiles in the region delimited by the red bracket in (A), show a marked change over line edge regions delimited by yellow dashed vertical lines in (A) (denoted as and ). Indicators define the core of the line, as well as the line edges instabilities due to a combination of overspray and de-wetting issues. Arrows are a guide for the eye.

$$\frac{dI ds}{dt} = -\frac{I g s}{\tau_e} \quad (1)$$

profile edge instability, i.e. percentage of OS and pinholes (indicated as OS-p) with respect to the whole line width (LW, indicated by the black double-headed line in figure 2(A)), defined as (hole-OS, hOS):

$$hOS \% = \frac{L_{OS-p}}{LW} \times 100, \quad (2)$$

### 3. Results and discussion

Figure 2(A) shows a SEM micrograph of a typical PEDOT:PSS AJP printed line (CGFR = 12, FR = 4, nozzle 100  $\mu\text{m}$ ). The effect of OS is clearly evidenced at the edges of PEDOT:PSS printed lines on Kapton as an undefined narrow profile (blue circle in figure 2(A)). This appears to be quite similar to what is reported for inks made of metallic nanoparticles [18], or adhesive inks [20], and experienced also in our lab. In this specific case, however, the edge of the line is further corrupted by the presence of pinholes (pointed by red arrows in figure 2(A)), i.e. discontinuities and defects along the sharp line profile. Pinholes are typically associated to the quality of the substrate surface, or to specific solvent/substrate interactions (aqueous PEDOT:PSS suspension interacting with a hydrophobic substrate) [36]. One way to remove pinholes is via an increasing of printing speed or a multi-layered printing. We verified that in our case the increasing of the printing speed leads to a worsening of the quality of the printed lines. (SI file, figure SI1). In order to better qualify the processes involved in PEDOT:PSS printing, we chose to characterize only one-pass printing line to guarantee a better control of the line thickness, since multi-layer printing does not imply a cumulative effect on the thickness increase. Figure 2(B) shows the typical line profile obtained by image analysis of the SEM micrographs. The cross-sectional profile of the printed PEDOT:PSS line shows a concave shape resembling to a ‘pudding-like’ form (rectangles with round shaped upper vertices). This kind of shape results to be a typical characteristic of PEDOT:PSS printed under different deposition conditions. To consider the presence of pinholes, we propose a different way to measure the

where, red circled zones in figure 2(B)) expresses the width of defective parts of the entire printed line.

The first step towards the evaluation of PEDOT:PSS lines quality requires the assessment of line widths at different fixed FR and as a function of CGFR, for the four nozzles used. Figure 3 shows the effect of CGFR on LW, where the horizontal dotted lines represent the nominal nozzle size (ND, nozzle diameter). Data acquisition was performed by holding a constant CGFR and varying FR upon changing the ShGFR. As expected, LW decreases for increasing FRs, as described by the equation [23]:

$$\frac{LW}{ND} = \sqrt{1 - \sqrt{\frac{FR}{1 + FR}}} \quad (3)$$

Even if equation (3) has been determined under some stringent approximations, it gives a good agreement, at least in terms of trends, with experimental data under laminar flow conditions, mainly at lower CGFRs and for inks based on low-volatile solvents [23]. For this reason, it is generally used for modelling quite different materials and substrates.

As shown in figure 3, our results confirm the predictions of equation (3) also in the case of PEDOT:PSS printed on Kapton, In particular:

1. LW decreases upon increasing the FR, confirming the effects of the confinement of the aerosol stream due to the role of the sheath gas;
2. the focussing effect  $LW < ND$  is observed for  $FR \geq 1$  at lower ND, while there are some

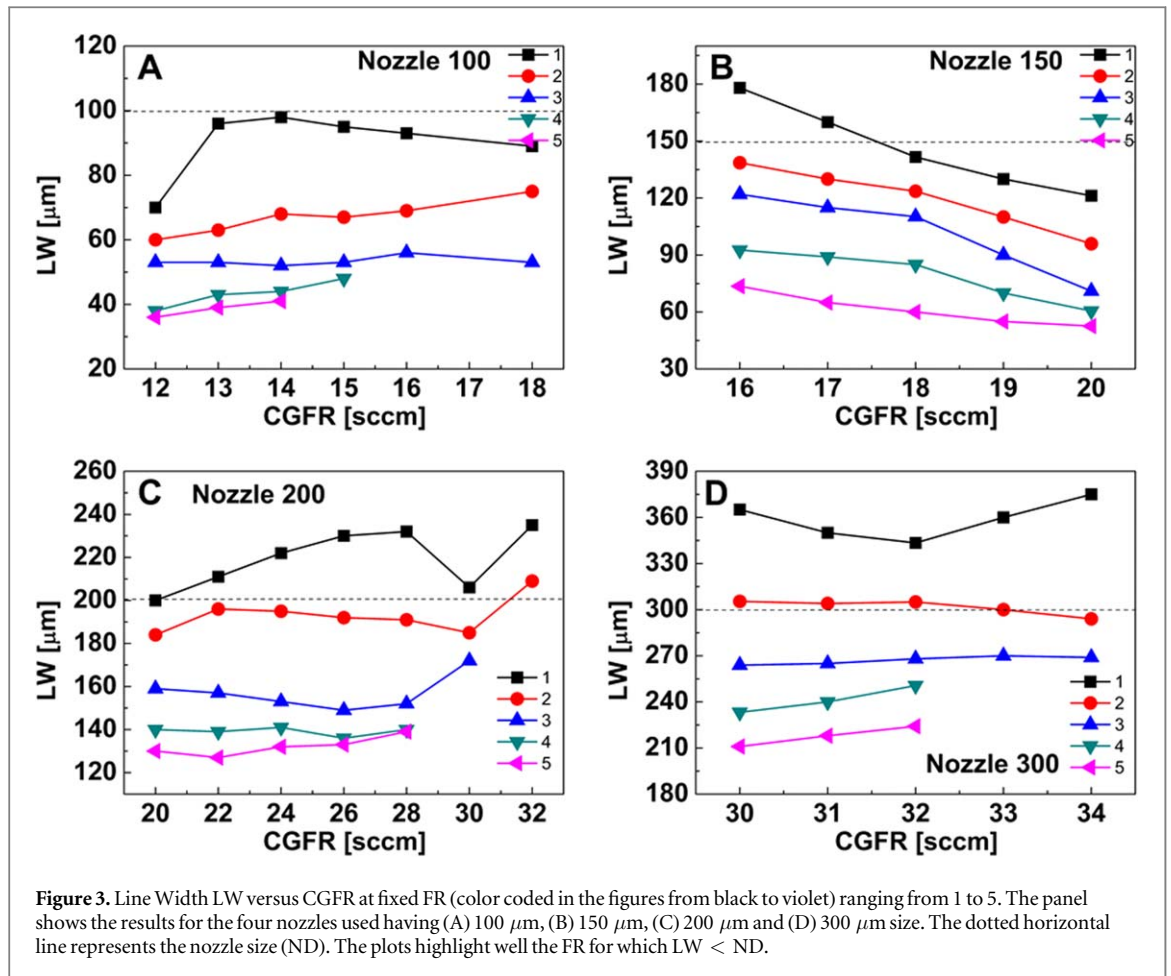


Figure 3. Line Width LW versus CGFR at fixed FR (color coded in the figures from black to violet) ranging from 1 to 5. The panel shows the results for the four nozzles used having (A) 100  $\mu\text{m}$ , (B) 150  $\mu\text{m}$ , (C) 200  $\mu\text{m}$  and (D) 300  $\mu\text{m}$  size. The dotted horizontal line represents the nozzle size (ND). The plots highlight well the FR for which  $LW < ND$ .

deviations at  $FR = 1$  for higher NDs (i.e. 200 and 300  $\mu\text{m}$ ). Such deviations are a fingerprint of  $hOS$  increase due to the arising of turbulences at  $FR = 1$ , where a weaker confinement by ShGFR is expected. In this case, in fact, it becomes probable that the aerosol stream can interact with surface defects at the nozzle exit, even though the laminar condition is generally fulfilled for typical AJP systems [20];

3. LW is not influenced by the magnitude of CGFR but it strongly depends on FR.

In figures 3(A)–(D) the points for which  $LW > ND$  can be considered outside the printability windows, because the line width is larger than the nominal nozzle diameter. For those points an OS-dominated printing regime takes place, as it is the case of  $FR = 1$  in 3 C and  $FR = 1$  and 2 in figure 3(D). Some points were not reported in the plots, especially for the highest values of  $FR = 4$  and  $FR = 5$  (ex. Nozzle 100,  $FR = 5$ ), because for those values the printing failed or went wrong, often because a too high sheath gas flow makes the nozzle clogged. An example of printed line dominated by OS is reported in figure SI2A (SI), together with the micrographs showing (i) two lines overlapped due to OS (figure SI2B), (ii) the region between adjacent lines in case of strong OS (figure SI2C) and

(iii) the dimensional analysis of ‘OS particles’ figure SI2D). Figure 3 represents hence the PEDOT:PSS printability window, that is the region where the line printed could be best defined as such.

Our  $hOS$  analysis (equation (2)) over the whole printed LW, carried out as described in the materials and methods section, is reported in figure 4. Here, the  $hOS$  is visualized using a polar representation where the angular coordinate represents the focus ratio (FR) and the radius length represents the  $hOS$  percentage with respect to the assessed LW. For a better readability, figure 4 reports the CGFR values corresponding to the highest and lowest  $hOS$ .

In this representation the closer are the experimental points to the centre of each circle, the lower is the percentage of  $hOS$  with respect to LW. The 300  $\mu\text{m}$  nozzle, compared to the other nozzles, shows minimum values of  $hOS$  over the widest range of FR. The maximum and minimum line widths and  $hOS$  are reported for all the analysed nozzles in table SI1 (SI) together with the CGFR and FR parameters realizing them.

The showed trends have been rationalized by Chen et al ([20] of the submitted manuscript) upon invoking some basic considerations coming from fluid dynamics principles.

In this work, a laminar flow of the aerosolized materials is always expected during the path of the

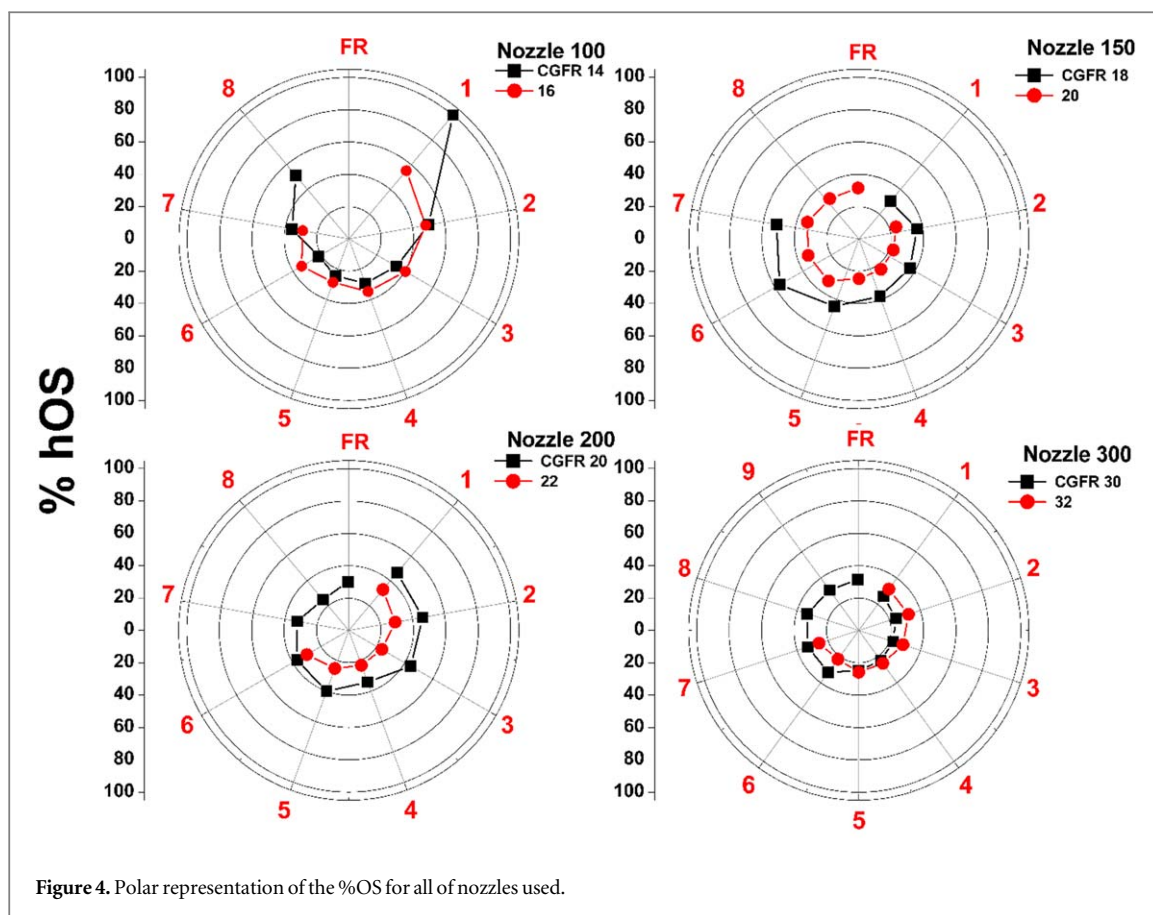


Figure 4. Polar representation of the %OS for all of nozzles used.

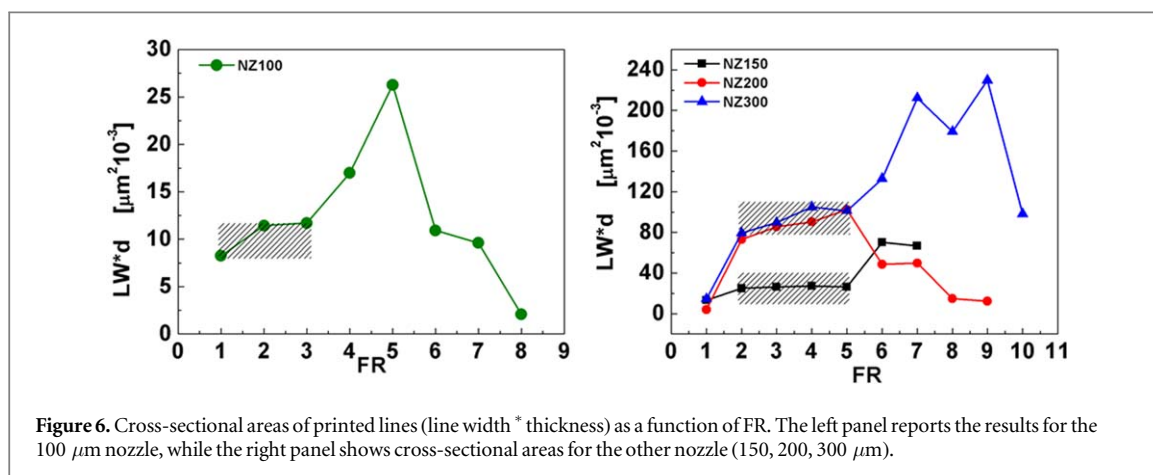
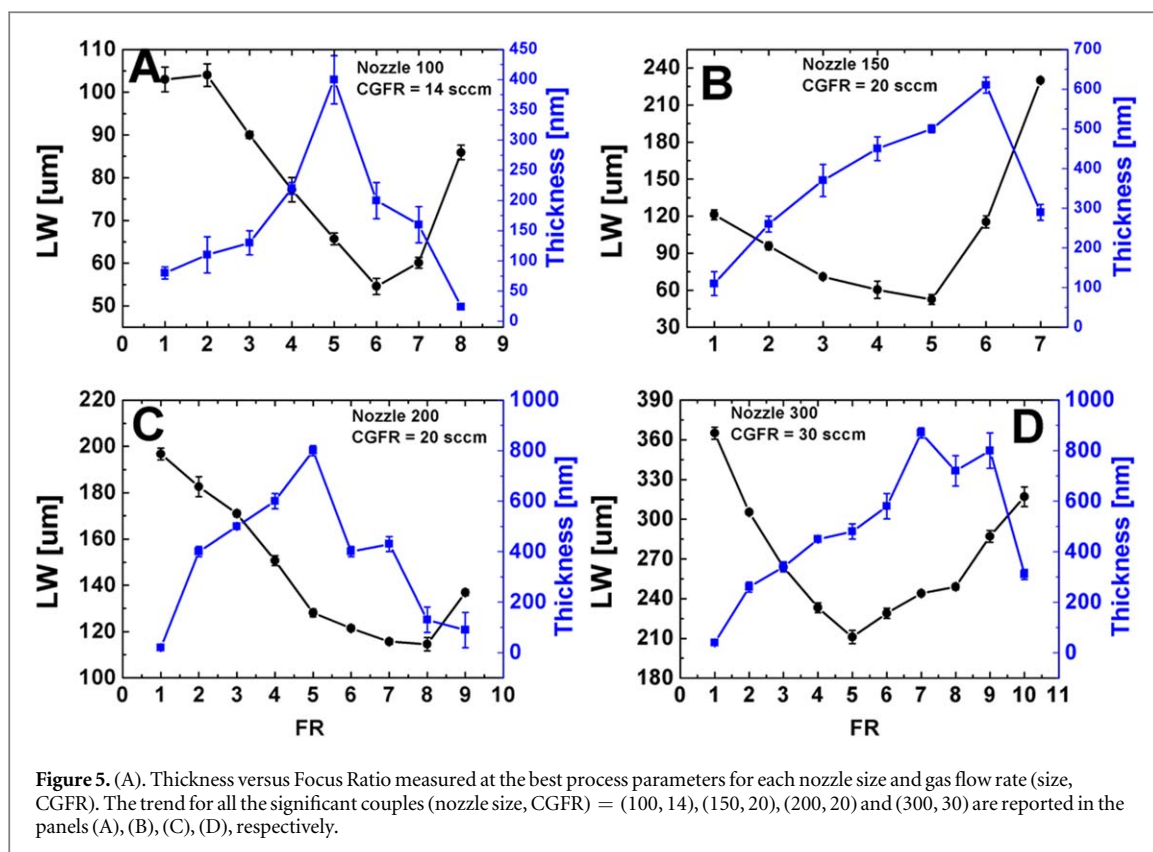
aerosol stream from the atomizer to the print head ( $Re < 2500$  under a pipe flow modelling) [20]. Nevertheless, other factors are important such as the design and state of the nozzle, the materials used and the surface treatments. Since the ideal case is far from being achieved in real cases, upon turbulences due to non-ideality of AJP systems, one would expect the formation in the aerosol of a non-uniform distribution of drops sizes around the nozzle axis. Smaller particles that have a significant component of the velocity perpendicular to the beam are therefore not efficiently confined by the sheath gas, and hence are generated away from the ideal nozzle axis. They tend to deviate from it when pushed by the carrier gas, giving rise to overspray issues. We have mentioned this study because, on one hand, typical parameters used for deposition by AJP systems are claimed to fulfil a condition of laminar flow and, on the other hand, we have effectively verified that OS is dramatically affected by the nozzles' state in so far as not perfectly cleaned nozzles imply an enhanced overspray.

Recently, the work by Secor [37] demonstrated that overspray can be ascribed to drying effects at the nozzle exit, without referring to turbulences arising from non-ideal conditions inside the aerosol path, and in particular at the nozzle exit. Experiments applied in the case of PEDOT:PSS ink with different ethylene glycol doping % are in progress.

We now discuss the line thickness dependence as a function of FR. As previously mentioned, also the

thickness of the printed lines was assessed considering FRs exceeding the printability window defined above. The best CGFR in terms of stability over the largest FR range was selected for each of the used nozzles. Figure 5 shows the width and thickness of the printed lines as a function of FR for the selected process parameters. We observe that the line thickness increases for decreasing width, in agreement with data reported in literature in the case of silver inks, confirming the idea of a focusing effect, according to which the total amount of material is the same and only the area over which it is deposited, changes [18]. In fact, for a given CGFR, the increase of ShGFR enhances the confinement effect of the gas stream, the LW decreases while the thickness increases (continuity equation). Hence, independently on the chosen nozzle, all the LW curves as a function of FR pass through a minimum FR value. This trend is mainly due to the increase of the %OS that enlarges the overall line width, confirming models proposed in literature for other materials [20].

A quantitative analysis indicates that the thickness of PEDOT:PSS lines spans over a wide range of values, from 10 nm (equal to a nominal monolayer of PEDOT grains in PEDOT:PSS suspension [38]) up to 900 nm, an overall range that is quite interesting for several applications including those based on supercapacitors [39, 40], and OECTs [41]. While in the case of printed silver lines the thickness (and LW) shows a monotonic trend, here the thickness) begins to fall (LW increases correspondingly) at FR around 5–7, confirming that at



too high FRs a printing regime where OS phenomena become too large takes place. Collected data, in addition, show that the largest, stable printing window within the explored FR range, was found for  $\text{ND} = 200 \mu\text{m}$  at  $\text{CGFR} = 20 \text{ sccm}$ . A careful analysis of the reported thickness versus FR curves, also indicates that the thickness of ( $\text{ND} = 150$ ,  $\text{CGFR} = 20$ ) and ( $\text{ND} = 300$ ,  $\text{CGFR} = 30$ ) both show similar values in the range of FR up to  $\text{FR} = 6$ , indicating that PEDOT:PSS lines with different widths and same thickness can be manufactured, whenever required.

Finally, by calculating the line cross section area of the printed features across different FR reported in figures 5(A)–(D), we have checked the range validity for the continuity equation. This check is needed as

the regime of validity of the continuity equation is not always valid for all FR defining the printed features [37]. In detail, we have calculated the values of the line cross-sectional areas approximating the line profile to a rectangular shaped cross-section. Results are summarized in the figure 6 and confirm that there is a range of FR for which the continuity equation is valid. We noticed that for the 100  $\mu\text{m}$  nozzle, the FR range of validity for the continuity condition is limited to FR varying from 1 to 3. For the other nozzles (150, 200 and 300  $\mu\text{m}$ ) we observed a plateau until  $\text{FR} = 5$ , above which the behavior is no more ideal. The deviation is realized (and experimentally confirmed by results in figures 4(A)–(D)) when the validity of equation (3) is no more guaranteed, i.e. when for a

given nozzle the line width shows a dependence on the carrier gas flow CGFR rather than on the focus ratio ( $FR = ShGFR/CGFR$ ).

As a final check of how printing condition may influence the conducting properties of PEDOT:PSS at the line level, we have assessed lines' conductivity upon different deposition conditions in the case of the 200  $\mu\text{m}$  nozzle. We printed Ag test patterns for 4-wire in-line probing, described in detail in a dedicated section in the supporting information file (section SI3). We found an average conductivity value of 154.3 ( $\pm 6.2$ , statistical error of the mean)  $\text{S cm}^{-1}$ , in good agreement with values reported by Heraeus in the data sheet of the row PEDOT:PSS formulation (Clevios P Jet N V2).

The ability to control geometrical features of printed lines and the knowledge of  $hOS$  weight on the line definition can be used to print organic transistors with finely tailored properties, depending on the applications they are devoted to. A case study is reported here, demonstrating the fabrication and characterization of a whole-OECTs with both the channel and the gate electrode made of PEDOT:PSS. OECTs are most frequently fabricated by a lithographic process [35], and recently also by Inkjet printing [4], mainly in applications for wearable or textile systems, where printing is essentially used for the deposition of organics. We recall that OECTs made of PEDOT:PSS are widely used in organic bioelectronics [41–45], mainly as highly performing biosensor [41, 46–49], textile [50–52], and recently for the detection of physiological signals (biopotentials) [21, 53–55]. They basically operate in depletion mode, meaning that the channel current  $I_{ds}$  decreases upon injection of cationic species from the electrolyte into the bulk of PEDOT:PSS channel [56, 57]. Here, we present the first set of OECTs fully printed by aerosol jet technique. The printed transistor is referred to hereinafter as AJP OECT. Worth to note that, while the nominal channel length is set at 200  $\mu\text{m}$  for all the fabricated AJP OECTs, the average value of the measured distance between source and drain contacts differs by less than 2% from the nominal value for all the fabricated devices (an optical image of source and drain electrodes spacing is reported as an example in figure SI4), indicating the high precision of the AJ200 printer. Table 2 reports the process parameters used for printing the three layers the OECT is composed of.

In figure 7 the schematics of the fabricated AJP OECTs (top and side views) and a real micrograph of the device designed for a 3-terminal ZIF connection, are reported.

Tests have been performed to assess the quality of printed PEDOT:PSS films via estimation of the material's pristine electrical current and charge carrier mobility. The baseline current ( $I_{ds}$ ) of pristine OECTs, measured in their dry state, that is before interfacing the channel with the electrolyte, shows a gaussian distribution centered at 0.33 mA and a standard

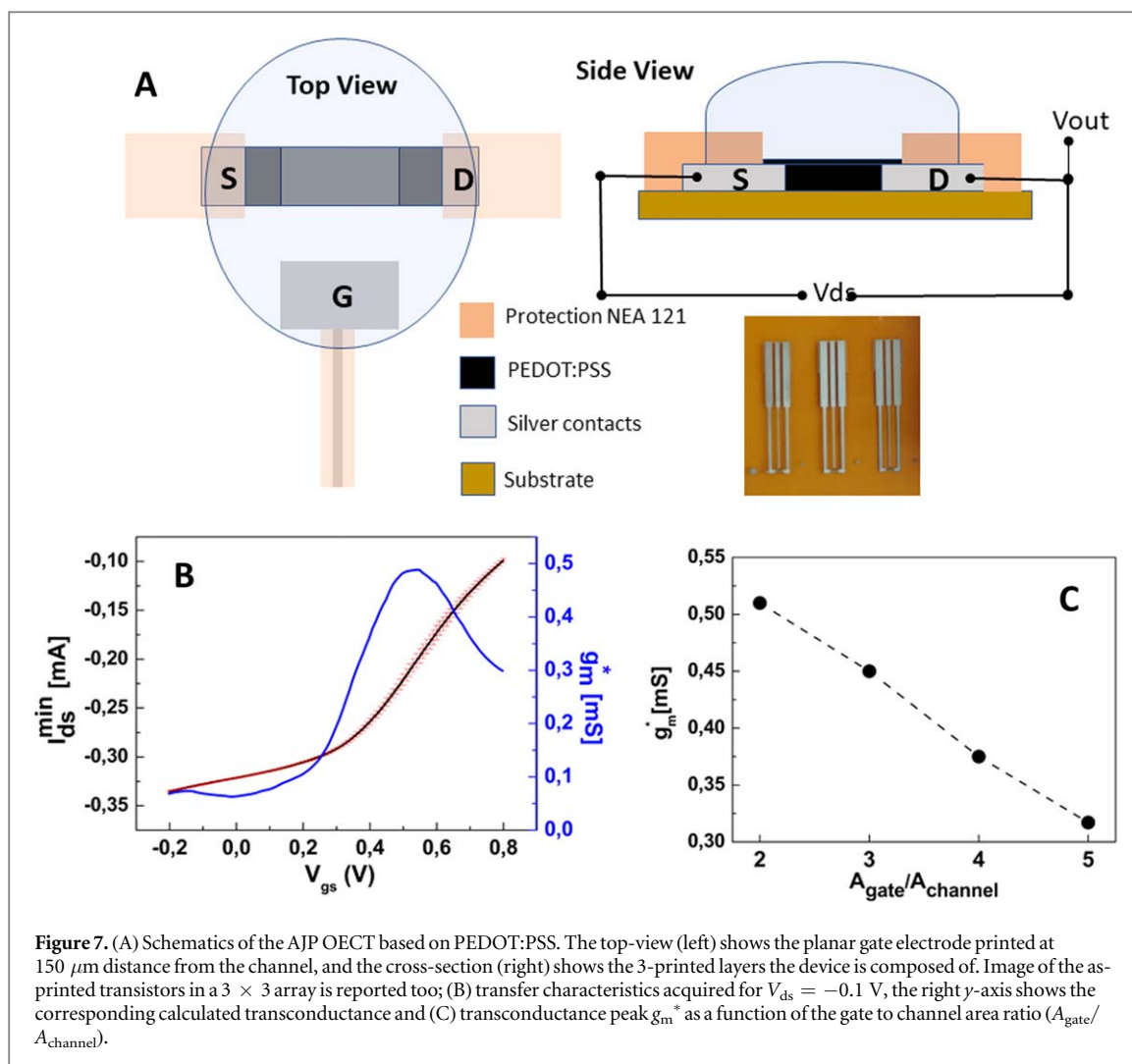
**Table 2.** Process parameters for AJP deposition of the three inks of silver, PEDOT:PSS and NEA 121 used in the fabrication of the OECTs. Sccm = standard cubic cm. Printing velocity = 1 mm  $\text{s}^{-1}$ .

Process parameters	Silver	PEDOT:PSS	
		Jet N V2	NEA 121
Nozzle size ( $\mu\text{m}$ )	150	200	300
Sheath gas (sccm)	40	60	50
Carrier flow (sccm)	20	30	1200
Exhaust flow (sccm) <sup>a</sup>	—	—	1150
Ultrasonic current (mA)	0.512	0.512	—
Platen Temperature ( $^{\circ}\text{C}$ )	50	60	0
Post-bake ( $^{\circ}\text{C}$ , time)	200, 1 h	120, 1 h	125, 10 min

<sup>a</sup> for pneumatic atomizer only.

deviation  $\sigma = 0.049$ , indicating a high reproducibility of the printing process. (Figure SI5A.) In addition, the holes transient time  $\tau_e$  calculated by driving the AJP OECT with the gate current (figure SI5B) is in the order of 12 ms (fit curve using equation (1) reported in figure SI5C), which corresponds to a charge carrier mobility in the range of  $10^{-4} \text{ cm}^2 \text{ V}^{-1} \text{ s}^{-1}$ , an order of magnitude lower than that of basic PEDOT:PSS formulation for cast deposited films [21, 34]. This difference is mainly due to the PEDOT:PSS formulation used for our printing systems which is less viscous but also less conductive than the basic one used in cast deposition. PEDOT:PSS. The transfer curve of figure 7(B), acquired for the OECT with 2:1, represents the curve statistically averaged on a total of nine measurements (three transfers for each of the AJP OECTs having the same channel/gate area ratio). The very low magnitude of error bars (statistical average error, SAE) shows high reproducibility also under OECT operation. The SAE is calculated as  $\sigma/\sqrt{N}$ , with  $N = 9$ . A typical output curve is reported for complete information in figure SI5D.

Current modulation upon  $V_{gs}$  driven cationic injection provides ON/OFF ratios between  $10^0$  and  $10^1$ , that is in line with the range of values expected for planar, all-PEDOT:PSS OECTs [48, 58–62]. The transconductance, defined as  $g_m = \Delta I_{ds}/\Delta V_{gs}$  is the main figure of merit of OECTs, expressing their amplification factor, or gain, upon transduction by PEDOT:PSS of ionic-signals into electronic ones [35]. Maximum device transconductance is  $\sim 0.5 \text{ mS}$  at  $V_{gs}$  of 0.3 V, retrieved for the 2:1 OECT, and in agreement with values reported in literature [47]. The peak of  $g_m$  linearly decreases with the increase of the gate to channel area ratios (figure 7(C)). The linear decrease suggests an additive contribution at the gate electrode that could be ascribed to the electroactive nature of PEDOT:PSS gate electrode exposed to the presence of Cl<sup>-</sup> ions in the electrolyte solution. If forced into the PEDOT:PSS bulk during the  $V_{gs}$  operation (mass transport), anions can change microstructural volumetric (hence, additive) capacitive contributions due



to electric double layers formed at the PEDOT cluster/PSS interface [63].

#### 4. Conclusions

We reported a systematic investigation of the aerosol jet technique applied to the printing of semiconducting PEDOT:PSS on a flexible film of Kapton substrate, demonstrating that it is a viable method well suited to flexible electronics applications. We demonstrated that critical parameters such as the width and thickness of the printed features could be quite nicely controlled in a range of significant interest for applications, giving a guide recipe for a proper PEDOT:PSS printing on Kapton as a function of nozzle sizes and printer's regulations.

Our study also includes a thorough assessment of the OS combined with emerged pinholes due to ink/substrate interaction, producing indications on how instabilities could be reduced by opportune choices of the printing process parameters. OS is a main cause of short-circuits or not-defined structures, reducing the final achievable printing resolution. The proposed original polar representation is particularly suitable for

an easy and immediate visualization of the OS trend and predicting the OS level given the printing parameters.

We finally demonstrated, as a case study leveraging on the obtained printing recipes, the fabrication of a whole-PEDOT:PSS, planar and flexible OEETs, to our knowledge printed for the first time with AJP technology. Their performance well compares to state of the art of PEDOT:PSS OEETs. We investigated the transconductance behaviour as a function of different device gate to channel area ratios, revealing a linear decrease of transconductance for increasing ratios.

We believe that our work, determining reliable optimal conditions for the direct writing of PEDOT:PSS, one of the most popular organic semiconductors, contributes to qualify AJP as a viable method, ideally suitable for organic flexible electronics applications.

#### Acknowledgments

This work was carried out in the joint laboratory 'Therseo Lab' between Camlin Italy Srl and IMEM—CNR Institute.

## ORCID iDs

Giuseppe Tarabella  <https://orcid.org/0000-0002-8898-714X>

## References

- [1] Caironi M and Noh Y-Y 2015 *Large Area and Flexible Electronics* (New York: Wiley) (<https://doi.org/10.1002/9783527679973>)
- [2] Soukup R, Navratil J, Reboun J and Richa T 2015 A comparison of the interdigital electrodes prepared by aerosol jet printing and lift-off technique *2015 38th Int. Spring Seminar on Electronics Technology (ISSE) (Piscataway, NJ)* (IEEE) pp 30–5
- [3] Gupta A A, Bolduc A, Cloutier S G and Izquierdo R 2016 Aerosol Jet Printing for printed electronics rapid prototyping *Proc.—IEEE Int. Symp. Circuits Syst.* July 2016 pp 866–9
- [4] Bihar E, Roberts T, Zhang Y, Ismailova E, Hervé T, Malliaras G G, De Graaf J B, Inal S and Saadaoui M 2018 Fully printed all-polymer tattoo/textile electronics for electromyography *Flex. Print. Electron* **3** 3
- [5] Gu Y, Hines D R, Yun V, Antoniak M and Das S 2017 Aerosol-jet printed fillets for well-formed electrical connections between different leveled surfaces *Adv. Mater. Technol.* **2** 1700178
- [6] Paulsen J A, Renn M, Christenson K and Plourde R 2012 Printing conformal electronics on 3D structures with aerosol jet technology *2012 Future of Instrumentation Int. Workshop (FIIW) Proc.* (Piscataway, NJ: IEEE) pp 1–4
- [7] Navratil J, Hamacek A, Reboun J and Soukup R 2015 Perspective methods of creating conductive paths by aerosol jet printing technology *2015 38th Int. Spring Seminar on Electronics Technology (ISSE) (Piscataway, NJ: IEEE)* 36–9
- [8] Kuang X, Roach D J, Wu J, Hamel C M, Ding Z, Wang T, Dunn M L and Qi H J 2019 Advances in 4D printing: materials and applications *Adv. Funct. Mater.* **29** 1805290
- [9] Seifert T, Sowade E, Roscher F, Wiemer M, Gessner T and Baumann R R 2015 Additive manufacturing technologies compared: morphology of deposits of silver ink using inkjet and aerosol jet printing *Ind. Eng. Chem. Res.* **54** 769–79
- [10] Hoey J M, Lutfurakhmanov A, Schulz D L and Akhatov I S 2012 A review on aerosol-based direct-write and its applications for microelectronics *J. Nanotechnol.* **2012** 1–22
- [11] Hong K, Kim S H, Mahajan A and Frisbie C D 2014 Aerosol jet printed p- and n-type electrolyte-gated transistors with a variety of electrode materials: exploring practical routes to printed electronics *ACS Appl. Mater. Interfaces* **6** 18704–11
- [12] Gupta A A, Arunachalam S, Cloutier S G and Izquierdo R 2018 Fully aerosol-jet printed, high-performance nanoporous ZnO ultraviolet photodetectors *ACS Photonics* **2018** 5 3923–9
- [13] Grunwald I, Groth E, Wirth I, Schumacher J, Maiwald M, Zoellmer V and Busse M 2010 Surface biofunctionalization and production of miniaturized sensor structures using aerosol printing technologies *Biofabrication* **2** 014106
- [14] Jing Q, Choi Y S, Smith M, Ou C, Busolo T and Kar-Narayan S 2019 Freestanding functional structures by aerosol-jet printing for stretchable electronics and sensing applications *Adv. Mater. Technol.* **4** 1900048
- [15] Zhang H, Moon S K and Ngo T H 2019 Hybrid machine learning method to determine the optimal operating process window in aerosol jet 3D printing *ACS Appl. Mater. Interfaces* **2019** **11** 17994–18003
- [16] Koch N, Chan C, Kahn A and Schwartz J 2003 Lack of thermodynamic equilibrium in conjugated organic molecular thin films *Phys. Rev. B* **67** 195330
- [17] Cummings J, Lowengrub J S, Sumpter B G, Wise S M and Kumar R 2018 Modeling solvent evaporation during thin film formation in phase separating polymer mixtures *Soft Matter* **14** 1833–46
- [18] Mahajan A, Frisbie C D and Francis L F 2013 Optimization of aerosol jet printing for high-resolution, high-aspect ratio silver lines *ACS Appl. Mater. Interfaces* **5** 4856–64
- [19] Salary R, Lombardi J P, Samie Tootooni M, Donovan R, Rao P K, Borgesen P and Poliks M D 2017 Computational fluid dynamics modeling and online monitoring of aerosol jet printing process *J. Manuf. Sci. Eng.* **139** 021015
- [20] Chen G, Gu Y, Tsang H, Hines D R and Das S 2018 The effect of droplet sizes on overspray in aerosol-jet printing *Adv. Eng. Mater.* **20** 1701084
- [21] Rivnay J et al 2015 High-performance transistors for bioelectronics through tuning of channel thickness *Sci. Adv.* **1** e1400251
- [22] Inal S, Rivnay J, Hofmann A I, Uguz I, Mumtaz M, Katsigiannopoulos D, Brochon C, Cloutier E, Hadziioannou G and Malliaras G G 2016 Organic electrochemical transistors based on PEDOT with different anionic polyelectrolyte dopants *J. Polym. Sci. B* **54** 147–51
- [23] Secor E B 2018 Principles of aerosol jet printing *Flex. Print. Electron.* **3** 035002
- [24] Cho J H, Lee J, Xia Y, Kim B, He Y, Renn M J, Lodge T P and Daniel Frisbie C 2008 Printable ion-gel gate dielectrics for low-voltage polymer thin-film transistors on plastic *Nat. Mater.* **7** 900–6
- [25] Jones C S, Lu X, Renn M, Stroder M and Shih W-S 2010 Aerosol-jet-printed, high-speed, flexible thin-film transistor made using single-walled carbon nanotube solution *Microelectron. Eng.* **87** 434–7
- [26] Xia Y, Zhang W, Ha M, Cho J H, Renn M J, Kim C H and Frisbie C D 2010 Printed Sub-2 V gel-electrolyte-gated polymer transistors and circuits *Adv. Funct. Mater.* **20** 587–94
- [27] Hong K, Kim S H, Lee K H and Frisbie C D 2013 Printed, sub-2V ZnO electrolyte gated transistors and inverters on plastic *Adv. Mater.* **25** 3413–8
- [28] Hong K, Kim Y H, Kim S H, Xie W, Xu W D, Kim C H and Frisbie C D 2014 Aerosol jet printed, Sub-2 v complementary circuits constructed from P- and N-type electrolyte gated transistors *Adv. Mater.* **26** 7032–7
- [29] Xie W, Zhang X, Leighton C and Frisbie C D 2017 2D insulator–metal transition in aerosol-jet-printed electrolyte-gated indium oxide thin film transistors *Adv. Electron. Mater.* **3** 1–6
- [30] Elschner A, Kirchmeyer S, Lovenich W, Merker U and Reuter K 2010 *PEDOT: principles and applications of an intrinsically conductive polymer* (Boca Raton, FL: CRC Press)
- [31] Cicoira F, Sessolo M, Yaghmazadeh O, DeFranco J A, Yang S Y and Malliaras G G 2010 Influence of device geometry on sensor characteristics of planar organic electrochemical transistors *Adv. Mater.* **22** 1012–6
- [32] Stavrinidou E, Leleux P, Rajaona H, Khodagholy D, Rivnay J, Lindau M, Sanaur S and Malliaras G G 2013 Direct measurement of ion mobility in a conducting polymer *Adv. Mater.* **25** 4488–93
- [33] D'Angelo P, Tarabella G, Romeo A, Marasso S, Verna A, Cocuzza M, Peruzzi C, Vurro D and Iannotta S 2018 PEDOT: PSS morphostructure and ion-to-electron transduction and amplification mechanisms in organic electrochemical transistors *Materials* **12** 9
- [34] Bernards D A and Malliaras G G 2007 Steady-state and transient behavior of organic electrochemical transistors *Adv. Funct. Mater.* **17** 3538–44
- [35] Khodagholy D, Malliaras G G, Rivnay J, Sessolo M et al 2013 High transconductance organic electrochemical transistors *Nat. Commun.* **4** 2133
- [36] Guan S W 2000 The selection, application and inspection of 100% solids polyurethane coatings for corrosion protection *Society for Protective Coatings (Tennessee (USA))* 1–8
- [37] Secor E B 2018 Guided ink and process design for aerosol jet printing based on annular drying effects *Flex. Print. Electron.* **3** 035007
- [38] Nardes A M, Kemerink M, Janssen R A J, Bastiaansen J A M, Kiggen N M M, Langeveld B M W, Van Breemen A J J M and De Kok M M 2007 Microscopic understanding of the anisotropic conductivity of PEDOT:PSS thin films *Adv. Mater.* **19** 1196–200

- [39] Cheng T, Zhang Y-Z, Zhang J-D, Lai W-Y and Huang W 2016 High-performance free-standing PEDOT:PSS electrodes for flexible and transparent all-solid-state supercapacitors *J. Mater. Chem. A* **4** 10493–9
- [40] Brooke R, Edberg J, Say M G, Sawatdee A, Grimoldi A, Åhlin J, Gustafsson G, Berggren M and Engquist I 2019 Supercapacitors on demand: all-printed energy storage devices with adaptable design *Flex. Print. Electron.* **4** 015006
- [41] Rivnay J, Inal S, Salleo A, Owens R M, Berggren M and Malliaras G G 2018 Organic electrochemical transistors *Nat. Rev. Mater.* **3** 17086
- [42] Lin P and Yan F 2012 Organic thin-film transistors for chemical and biological sensing *Adv. Mater.* **24** 34–51
- [43] Tarabella G, Mahvash Mohammadi F, Coppède N, Barbero F, Iannotta S, Santato C and Cicoira F 2013 New opportunities for organic electronics and bioelectronics: ions in action *Chem. Sci.* **4** 1395
- [44] Berggren M and Richter-Dahlfors A 2007 Organic bioelectronics *Adv. Mater.* **19** 3201–13
- [45] Rivnay J, Owens R M and Malliaras G G 2014 The rise of organic bioelectronics *Chem. Mater.* **26** 679–85
- [46] Tang H, Lin P, Chan H L W and Yan F 2011 Highly sensitive dopamine biosensors based on organic electrochemical transistors *Biosens. Bioelectron.* **26** 4559–63
- [47] Gualandi I, Tonelli D, Mariani F, Scavetta E, Marzocchi M and Fraboni B 2016 Selective detection of dopamine with an all PEDOT:PSS organic electrochemical transistor *Sci. Rep.* **6** 35419
- [48] Romeo A, Tarabella G, D'Angelo P, Caffarra C, Cretella D, Alfieri R, Petronini P G and Iannotta S 2015 Drug-induced cellular death dynamics monitored by a highly sensitive organic electrochemical system *Biosens. Bioelectron.* **68** 791–7
- [49] Jimison L H, Tria S A, Khodagholy D, Gurfinkel M, Lanzarini E, Hama A, Malliaras G G and Owens R M 2012 Measurement of barrier tissue integrity with an organic electrochemical transistor *Adv. Mater.* **24** 5919–23
- [50] De Rossi D 2007 A logical step *Nat. Mater.* **6** 328–9
- [51] Hamed M, Forchheimer R and Inganäs O 2007 Towards woven logic from organic electronic fibres *Nat. Mater.* **6** 357–62
- [52] Gualandi I, Marzocchi M, Achilli A, Cavedale D, Bonfiglio A and Fraboni B 2016 Textile organic electrochemical transistors as a platform for wearable biosensors *Sci. Rep.* **6** 33637
- [53] Khodagholy D, Doublet T, Quilichini P et al 2013 In vivo recordings of brain activity using organic transistors *Nat. Commun.* **4** 1575
- [54] Campana A, Cramer T, Simon D T, Berggren M and Biscarini F 2014 Electrocardiographic recording with conformable organic electrochemical transistor fabricated on resorbable bioscaffold *Adv. Mater.* **26** 3874–8
- [55] Leleux P, Rivnay J, Lonjaret T, Badier J M, Bénar C, Hervé T, Chauvel P and Malliaras G G 2015 Organic electrochemical transistors for clinical applications *Adv. Healthc. Mater.* **4** 142–7
- [56] Bernardis D A, Macaya D J, Nikolou M, DeFranco J A, Takamatsu S and Malliaras G G 2008 Enzymatic sensing with organic electrochemical transistors *J. Mater. Chem.* **18** 116–20
- [57] Tarabella G, Santato C, Yang S Y, Iannotta S, Malliaras G G and Cicoira F 2010 Effect of the gate electrode on the response of organic electrochemical transistors *Appl. Phys. Lett.* **97** 123304
- [58] Blaudeck T, Ersman P A, Sandberg M, Heinz S, Laiho A, Liu J, Engquist I, Berggren M and Baumann R R 2012 Simplified large-area manufacturing of organic electrochemical transistors combining printing and a self-aligning laser ablation step *Adv. Funct. Mater.* **22** 2939–48
- [59] Mattana G, Loi A, Woytasik M, Barbaro M, Noël V and Piro B 2017 Inkjet-printing: a new fabrication technology for organic transistors *Adv. Mater. Technol.* **2** 1–27
- [60] Mattana G, Briand D, Marette A, Vásquez Quintero A and De Rooij N F 2015 Polylactic acid as a biodegradable material for all-solution-processed organic electronic devices *Org. Electron. Phys., Mater. Appl.* **17** 77–86
- [61] Faddoul R, Coppard R and Berthelot T 2014 Inkjet printing of organic electrochemical immunosensors *SENSORS (Valencia, December 2014)* (IEEE) pp 1088–91
- [62] Basiric L, Cosseddu P, Scidà A, Fraboni B, Malliaras G G and Bonfiglio A 2012 Electrical characteristics of ink-jet printed, all-polymer electrochemical transistors *Org. Electron. Phys., Mater. Appl.* **13** 244–8
- [63] Volkov A V, Wijeratne K, Mitraka E, Ail U, Zhao D, Tybrandt K, Andreasen J W, Berggren M, Crispin X and Zozoulenko I V 2017 Understanding the capacitance of PEDOT:PSS *Adv. Funct. Mater.* **27** 1700329